Stable cycling of Si nanowire electrodes in fluorine-free cyano-based ionic liquid electrolytes enabled by vinylene carbonate as SEI-forming additive

Niyousha Karimi [a,b], Maider Zarrabeitia [a,b], Hugh Geaney [c], Kevin M. Ryan [c], Boyan Iliev [d], Thomas J.S. Schubert [d], Alberto Varzi [a,b,*], Stefano Passerini [a,b,**]

[a] *Helmholtz Institute Ulm (HIU), Helmholtzstrasse 11, 89081, Ulm, Germany*
[b] *Karlsruhe Institute of Technology (KIT), P.O. Box 3640, 76021, Karlsruhe, Germany*
[c] *Department of Chemical Sciences and Bernal Institute, University of Limerick, Limerick, V94 T9PX, Ireland*
[d] *IoLiTec-Ionic Liquids Technologies GmbH, Im Zukunftspark 9, 74076, Heilbronn, Germany*

HIGHLIGHTS

- Cyano-based Ionic liquid (IL) electrolytes are studied with Si nanowire anodes.
- Vinylene carbonate (VC) is investigated as SEI forming additive.
- VC helps reducing IL decomposition and controlling SEI growth.
- The resulting SEI has a layered structure including inorganic and organic species.
- Si nanowire anodes deliver in such F-free electrolyte 1500 mAh g^{-1} after 500 cycles.

GRAPHICAL ABSTRACT
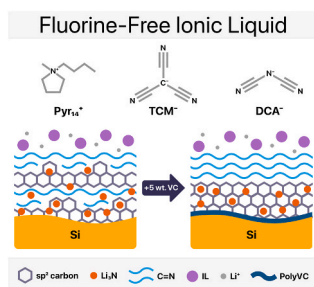
ABSTRACT

Herein, the mixture of the fluorine-free cyano-based ionic liquid N-butyl-N-methylpyrrolidinium tricyanomethanide (Pyr$_{14}$TCM), lithium dicyanamide (LiDCA) (1:9 salt:IL mole ratio) and 5 wt% vinylene carbonate (VC) is proposed as an electrolyte for the stable electrochemical alloying of silicon nanowire (Si NW) anodes. Detailed electrochemical characterization of the electrolyte (long-term galvanostatic cycling and impedance tests of Si NW-Li half-cells) demonstrates a remarkable cycling performance of the Si anode delivering 1500 mAhg^{-1} after 500 cycles with 99.5% Coulombic efficiency. The electrode/electrolyte interface is thoroughly investigated via scanning electron microscopy (SEM), energy dispersive X-ray (EDX) mapping, and X-ray photoelectron spectroscopy (XPS). The postmortem analysis reveals the key role of VC in controlling the IL decomposition, resulting in a bilayer solid electrolyte interphase (SEI) formation. The inner layer is mostly composed of graphitic carbon serving as a conductive coating for Si, and inorganic compounds such as Li$_3$N providing high Li-ion conductivity. The outer-layer, is rich in polymeric species ensuring the good mechanical stability and flexibility to withstand the extreme volume change of Si during de-/alloying process, thus explaining the observed prolonged cycling performance.

* Corresponding author. Helmholtz Institute Ulm (HIU), Helmholtzstrasse 11, 89081, Ulm, Germany.
** Corresponding author. Helmholtz Institute Ulm (HIU), Helmholtzstrasse 11, 89081, Ulm, Germany.
E-mail addresses: alberto.varzi@kit.edu (A. Varzi), stefano.passerini@kit.edu (S. Passerini).

1. Introduction

Lithium-based systems currently dominate battery markets from electric vehicles to portable electronics. Given the continuously growing volume of such markets, factors such as safety, production costs and environmental impact during production and recycling are of crucial importance when it comes to designing new battery materials [1–6].

The electrolytes used in commercial lithium ion batteries (LIBs) are mixtures of linear (e.g., dimethyl carbonate (DMC), diethyl carbonate (DEC), and ethyl methyl carbonate (EMC)) and cyclic (e.g., ethylene carbonate (EC)) carbonates as solvents and lithium hexa-fluorophosphate ($LiPF_6$) as conducting salt. However, there are major drawbacks and safety hazards associated with these electrolytes. For instance, the organic carbonate solvents are highly flammable [7]. Additionally, $LiPF_6$ suffers from relatively low thermal stability [8,9] and is highly sensitive to water. In fact, even trace amount of moisture result in defluorination reactions, forming compounds such as PF_5 and HF, which are known to be toxic and corrosive and have a detrimental influence on the battery performance [10,11]. From this point of view, fluorine-free electrolytes [12–14], in particular fluorine-free ionic liquids, have shown promising results [15,16].

Ionic liquids (ILs), which are molten salts at room temperature, represent a safer alternative class of electrolyte solvents owing to their inherently low volatility and wide temperature stability [17–19]. In particular, cyano-based ILs such as $Pyr_{14}TCM$, exhibit low viscosity, high ionic conductivity, and low density compared to the well-established fluorinated ILs such as bis(trifluoromethanesulfonyl) imide (TFSI)- and bis(fluoromethanesulfonyl)imide (FSI)-based ILs [15, 20–22]. This can potentially lead to increased safety, coupled with lower production costs due to the absence of the fluorination step during electrolyte production [12,15].

In this work the focus is placed on the binary mixture of $Pyr_{14}TCM$ and LiDCA (1:9 mole ratio), following our previous study wherein the physico-chemical and electrochemical characteristics of N-butyl-N-methylpyrrolidinium dicyanamide ($Pyr_{14}DCA$) and $Pyr_{14}TCM$ were comprehensively investigated [16]. The study revealed that a mixed anion electrolyte (LiDCA-$Pyr_{14}TCM$ in 1:9 mole ratio) formed the thinnest and the most homogenous solid electrolyte interphase (SEI) on Li metal electrode, resulting in improved electrochemical performance compared to single-anion electrolyte systems. Additionally, the electrolyte also exhibited high ionic conductivity (4.9 mS cm^{-1} at 20 °C) [16].

Following these promising results, we extend here the study to the high capacity silicon anodes. Si is amongst the most promising anode materials for the next generation of LIBs [23,24]. However, the application of "pure" elemental Si still remains a challenge to overcome due to the extensive volume variation of up to 280%, which induces a great mechanical stress on the composite electrode [25]. Nonetheless, Si has already been incorporated, up to ca.8 wt%, in graphite anodes to boost the energy and power density of commercial batteries [25,26].

For this study, Sn seeded Si NWs synthesized directly from the stainless-steel current collector were selected as a model system. This eliminated any influence from binder and/or conductive additives, enabling a more accurate investigation of the impact of the electrolyte on the electrochemical performance and SEI morphology and composition. We present the cycling performance of Si NW electrodes in IL electrolyte (LiDCA-$Pyr_{14}TCM$ 1:9 mole ratio) with and without the electrolyte additive vinylene carbonate (VC, 5 wt%). Electrochemical impedance spectroscopy (EIS), scanning electron microscopy (SEM), energy dispersive X-ray spectroscopy (EDX), and X-ray photoelectron spectroscopy (XPS) have been employed to comprehensively probe the characteristics of the electrode/electrolyte interphase upon cycling. To the best of our knowledge, no other work on the application of fluorine-free ILs for Si-based anodes is available.

2. Experimental

Electrolyte preparation: $Pyr_{14}TCM$, $Pyr_{14}DCA$ and LiDCA were supplied by IoLiTec GmbH. The three materials were dried following the procedure previously reported [16]. The water content of the ILs was determined lower than 20 ppm by coulometric Karl Fischer titration (Mettler-Toledo Titrator Compact C30; detection limit 10 ppm). All dried samples were directly transferred into an Ar filled glove-box (LabMaster, Mbraun GmbH, Germany, $O_2 < 0.1$ ppm, $H_2O < 0.1$ ppm) for storage and cell assembly. Vinylene carbonate (VC, 99.5%) was purchased from Merck and used as received. The electrolyte solutions LiDCA-$Pyr_{14}TCM$ (salt:IL = 1:9 mole ratio, referred to as ILE thereafter) and LiDCA-$Pyr_{14}TCM$+ 5 wt% VC (weight percent with respect to the total weight of the solution, referred to as ILE + VC thereafter) were prepared and stored inside the glove-box. Fig. S7 in Supporting Information displays the structure of the ions constituting the investigated ILs.

Si NW anode preparation: Sn seeded Si NW anodes were fabricated using a solvent vapour growth system. The preparation method was discussed in full detail previously [27,28]. In this case, a 20 nm thick Sn layer was thermally evaporated onto a 12 mm stainless steel disk. The growth substrates were then placed in a long-neck Pyrex round bottom flask containing 7 ml of squalane (Sigma Aldrich, 99%). The flask was connected to an argon line via a water condenser, placed inside an up-right furnace and heated to 460 °C. Subsequently, 0.75 ml of phenyl-silane (Sigma Aldrich, 97%) precursor was injected into the system through a septum cap. After 1 h, the reaction was terminated and the setup was allowed to cool to room temperature.

Prior to use, the electrodes discs were further vacuum-dried for 12 h it 100 °C. The electrodes were then transferred to an argon-filled glove-box (LabMaster, Mbraun GmbH, Germany, $O_2 < 0.1$ ppm, $H_2O < 0.1$ ppm) for storage and cell assembly. The active mass loading of the electrodes ranged from 0.1 to 0.2 mg cm^{-2}.

Electrochemical tests: For the electrochemical characterization, three-electrode Swagelok® cells were used. The cell assembly was carried out in an argon-filled glove box using Si NW electrode as working electrode (WE) and metallic Li foil (99% battery grade, Honjo Metal, Japan) as counter and reference electrodes (CE and RE). The electrodes were separated by a glass fiber felt (Whatman GF/D grade) soaked with 130 μl of the IL electrolyte (ILE and ILE + VC). All measurements were conducted at 20 ± 2 °C using climatic chambers (Binder). The Si/Li half-cells were investigated through galvanostatic cycling experiments within 0.01 and 2 V vs. Li/Li$^+$ potential range at C/20 (1C = 3579 mA g^{-1}) for the first cycle and C/10 for the following using a battery cycler (Maccor 4000, USA). Electrochemical impedance spectroscopy (EIS) measurements were performed on Si/Li half-cells in three-electrode cell configuration via a VMP-3 potentiostat (Biologic Science Instruments). The impedance spectra were recorded upon cycling (after each full charge/discharge cycle) at OCV conditions in the frequency range of 1 MHz–10 mHz, by applying a 10 mV amplitude voltage.

2.1. Postmortem analysis

The morphology of the Si NW electrodes surface after the first cycle in ILE or ILE + VC and the 100th cycle in ILE + VC, was characterized by scanning electron microscopy (SEM; Zeiss LEO 1550 microscope). The cells were disassembled inside the glove box. The recovered electrodes were rinsed with dimethylcarbonate (DMC) to remove the residual IL and dried for 2 h inside the glove box antechamber under vacuum. The electrodes were then transferred to the SEM chamber via an air-tight transfer box preventing exposure to air.

X-ray photoelectron spectroscopy (XPS) experiments were performed on the Si NW electrodes after the first cycle in ILE or ILE + VC. The cells were disassembled inside the glove box. The electrodes were rinsed with DMC and dried before transfer to the XPS using an air-tight vessel to prevent contact with air or moisture. Although DMC is known

to form carbonate compounds upon decomposition on the electrode's surface, thus introducing artifacts to the SEI composition, the additional rinsing step for sample preparation is inevitable. In fact, the large amount of IL remaining on the electrode's surface, makes it effectively inaccessible even after prolonged sputtering time. Indeed, the Ar^+ sputtering method to remove the IL traces is more invasive, which can induce more alterations in the SEI. Finally, DMC is the most common solvent used in literature for removing the traces of ionic liquid from the electrode's surface for post-mortem analysis [29–31]. For the measurements, a monochromatic Al Kα (hν = 1.487 eV) X-ray source and the Phoibos 150 XPS spectrometer (SPECS –Surface Concept) equipped with a micro-channel plate and Delay Line Detector (DLD) were used. The scans were acquired in a Fixed Analyzer Transmission mode with an X-ray source power of 200 W (15 kV), 30 eV pass energy and 0.1 eV energy steps. The fitting of the experimental spectra was performed with the CasaXPS software, using a nonlinear Shirley-type background and 70% Gaussian and 30% Lorentzian profile functions. Due to absence of a clear hydrocarbon peak in C 1s spectra commonly selected as reference, the binding energy scale was set to N^+ 1s peak (i.e., positive nitrogen from the pyrrolidinium ring) equal to 402 eV [32]. Additionally, the binding energy separations (ΔBEs) of each species observed in different elements was determined ensuring the correctness of the peak fitting, as was previously carried out for other Li-battery compounds [16,33].

3. Result and discussion

3.1. Electrochemical performance of Si NW electrodes in fluorine-free IL electrolyte

The reversibility of Li alloying/dealloying process for the Si NW anode in ILE was studied by galvanostatic cycling. Fig. 1 displays the potential vs. capacity profiles, the corresponding differential capacity plot, and capacity/Coulombic efficiency vs. cycle number. As shown in Fig. 1a, the first cycle was performed at a slower C-rate (0.02C) to allow for the proper formation of the SEI layer, while the following cycles were performed at a higher C-rate, i.e., 0.1C. The first lithiation and delithiation capacities were 1732 mA h g $^{-1}$ and 730 mA h g $^{-1}$, respectively, yielding a Coulombic efficiency of 42%. Despite the low capacities and Coulombic efficiency, the differential capacity profile of the first cycle (Fig. 1b) shows the characteristic features of crystalline Si (c-Si) lithiation process. The main peak at 0.1 V arises from the two-phase region where c-Si reacts with Li to form an amorphous lithium silicide (a-Li_xSi) [34,35]. This peak is observable in the potential profile as the long sloping plateau (Fig. 1a). The differential capacity plot also reveals the presence of several small peaks below 1 V corresponding to the shoulder observed in the first lithiation profile, and a very small peak at 20 mV arising from c-$Li_{15}Si_4$ phase formation [35–39]. Upon delithiation, two peaks appearing at 0.32 V and 0.5 V correspond to delithiation plateaus of amorphous Si, while the peak at 0.45 V is related to the delithiation of the c-$Li_{15}Si_4$ phase which disappears in the following cycles. From the second cycle, the capacity dropped to 400 mA h g $^{-1}$ and kept rapidly fading until 130 mA h g $^{-1}$ after 100 cycles (Fig. 1c). The clear lithiation/delithiation peaks of amorphous Si observed in the differential capacity plot (inset in Fig. 1b) indicate that the alloying process still takes place, however, the poor cycling performance could potentially be due to the absence of an effective SEI layer on the Si NWs.

To promote the formation of a stable SEI layer on Si NWs, 5 wt % VC was added to the electrolyte. The use of VC as an additive was recently reported in a study of Stokes et al., which demonstrated VC to be the best performing amongst possible non-fluorinated additives [28]. The use of an organic additive should not affect the overall safety of the cell, as the small amount present in the electrolyte should mostly be consumed during the first half cycle (lithiation) [40,41].

Results obtained from the galvanostatic cycling test of Si anode in ILE + VC are reported in Fig. 2, showing a significant performance improvement. The first lithiation profile (run at 0.02C) differs
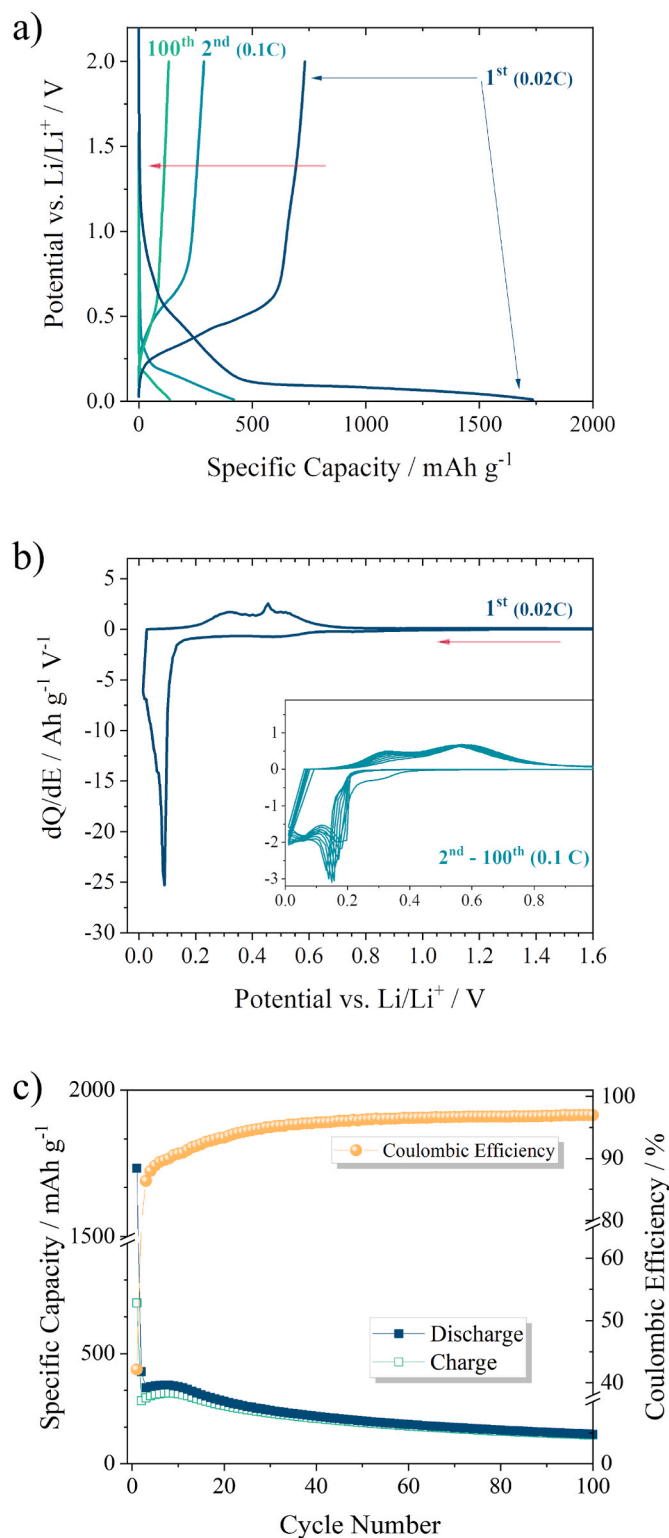

Fig. 1. a) potential profile vs capacity, b) differential capacity vs potential, and c) the evolution of lithiation/delithiation capacity and Coulombic efficiency vs cycle number of Li/Si half-cells in ILE. The first full cycle was carried out at 0.02C, whereas the following cycled were run at 0.1C at 20 °C.

substantially from the following cycles (as shown in Fig. 2a), displaying a shoulder at 1.1 V (also marked in dQ/dV plot in Fig. 2b) followed by a flat plateau at about 0.1 V, indicative of Li-alloying in c-Si. The observed shoulder matches the voltage reported for decomposition of VC [42]. Note that the absence of such feature in the subsequent cycles suggests
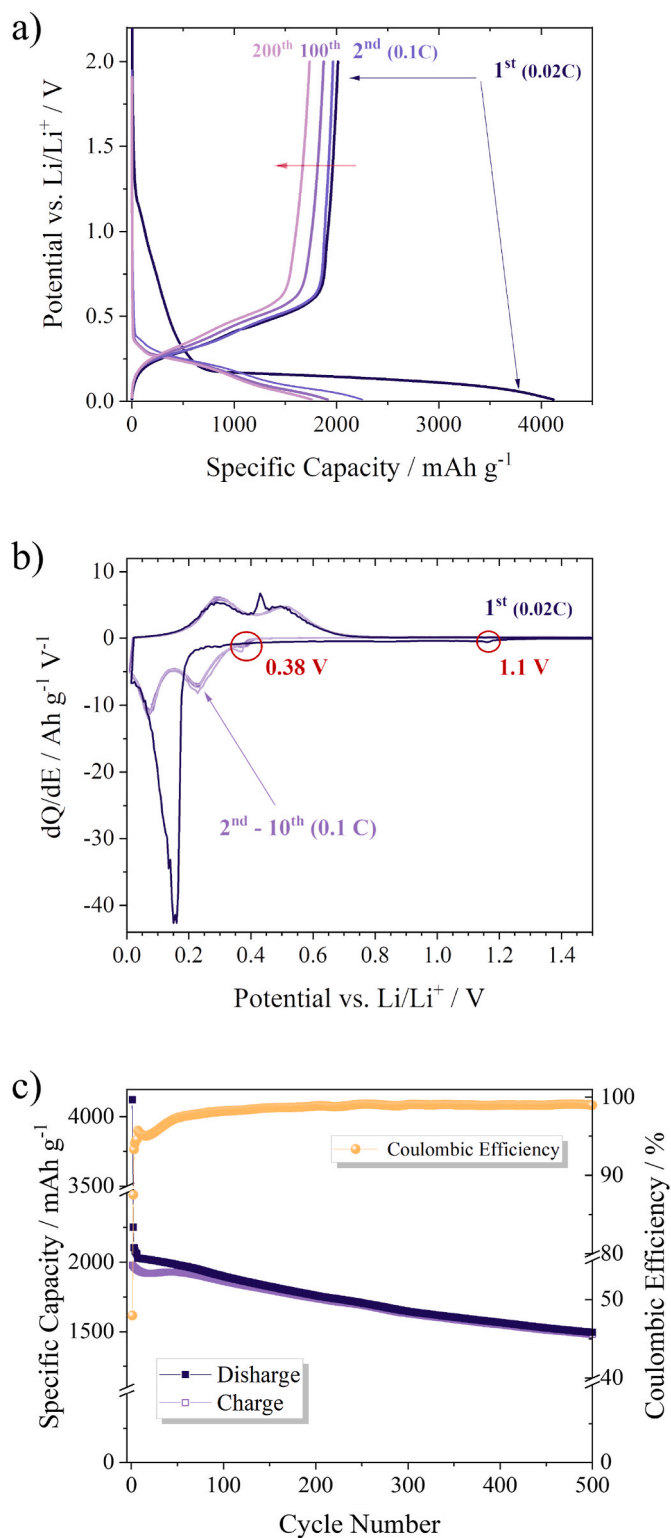
Fig. 2. a) potential profile vs capacity, b) differential capacity vs potential, and c) the evolution of delithiation/lithiation capacity and Coulombic efficiency vs cycle number of Li/Si half-cells in ILE + VC. The first full cycle was carried out at 0.02C, whereas the following cycled were run at 0.1C at 20 °C.

the complete consumption of VC during the first lithiation cycle. However, this behavior could also be explained by the formation of a very strong SEI capable of withstanding the volumetric changes of lithiated Si, i.e., preventing the exposition of fresh Si to the electrolyte and the further decomposition of remaining VC.

During delithiation, both the potential profile and the corresponding differential capacity plot replicate the features recorded for the Si anode in ILE (VC-free). The first cycle capacity values for lithiation and delithiation were 4125 mA h g^{-1} and 2016 mA h g^{-1}, respectively, which correspond to a Coulombic efficiency of 48.8%. Since the capacity loss due to decomposition of VC was determined to be about 6% (270 mA h g^{-1} based on the peak area in the differential capacity curve), the remaining capacity loss (45%) could be associated with other factors such as electrolyte reaction with the native SiO$_2$ layer [43], or surface degradation exposing fresh Si surface to the electrolyte [44]. Detailed discussion regarding the morphology and composition of SEI layer is presented in the following section (see part 3.2). It should be noted though, that relatively low first-cycle Coulombic efficiencies are not unexpected for Si NW anodes. In fact, values below 80% are quite common [39,41,45–48]. This low efficiency can be explained by the large interfacial contact area between the electrolyte and the nano-sized active material, leading to extensive SEI layer formation and low Coulombic efficiency [39].

In the following lithiation half-cycles (at 0.1C) the two plateaus appearing at 0.22 V and 0.1 V(see Fig. 2b) are characteristic of Li alloying with amorphous Si, while those two at 0.3 V and 0.5 V during delithiation arise from the corresponding reverse processes. The additional peak observed during lithiation at 0.38 V coincides with the lithiation of Sn seeds, suggesting that these seeds remain in electrical contact with Si NWs during cycling (Fig. S1 in supporting information). However, the peak associated with the dealloying of Li$^+$ from Sn, which should appear above 0.5 V, could not be identified, hence suggesting that the process is irreversible. The reappearance of Sn lithiation peak in the following cathodic scans is, however, quite unexpected. Although we do not have a direct explanation for such phenomenon, it could be speculated that in each cycle new Sn seeds become electrochemically active as result of the active material (Si) rearrangement in the electrode allowing the electrical contacting of the Sn seeds that were previously disconnected. The capacity associated with the lithiation of the Sn seeds was determined from the peak area in the differential capacity curve to be quite small (marked in Fig. 2b), corresponding to about 3% of the total delivered capacity. Although such contribution is minimal and decreases with cycling, it could be partially responsible for the Coulombic efficiency not exceeding 99.5% during the cycling test.

The long-term cycling test of the Si NW anode (Fig. 2c) depicts an increase in Coulombic efficiency in the second cycle to 87%, and around 96% during the following 30 cycles. Following, the cycling stability improves over time, with Coulombic efficiency converging to 99.5% after 100 cycles. This indicates that, eventually, a stable SEI layer is formed in the fluorine-free ILE + VC, despite the extreme volume changes of the Si anode during the lithiation and delithiation processes. Overall, reversible capacities of 1760 mA h g^{-1} after 200 cycles and 1500 mA h g^{-1} after 500 cycles are recorded (Fig. 2c), corresponding to, respectively, 88% and 75% retention with respect to the second cycle delithiation capacity. Previously, we have reported the performance of similar Si NW electrodes in carbonate and F-containing IL electrolytes [28,54]. The characteristics of these electrodes (synthesis regimes, mass loadings etc.) are comparable and allow a thorough comparison of their performance based on the electrolyte compositions. Overall the capacity values here compare well with our previous studies in alternative electrolytes (with and without VC as the SEI forming additive). A comparison can be made after 250 cycles, as our previous studies employed this cutoff for cycle number. Based on the base electrolyte of 0.1LiTFSI-0.6-PYR13FSI-0.3PYR13TFSI, the specific capacity was approximately 1100 mAhg^{-1} after 250 cycles without VC and 1600 mAhg^{-1} with 5% VC [28]. For carbonate-based electrolytes, the Si nanowire electrode delivered only 250 mAhg^{-1} after 250 cycles, while the addition of 3% VC boosted the capacity to 1300 mAhg^{-1} [54]. In this work, the capacity of the electrode after 250 cycles in the VC containing electrolyte is ca. 1700 mAhg^{-1}. Therefore, it outperforms both the carbonate electrolyte as well as the costly F-containing IL. It should also be noted that the

stability of the cell in the current study was sufficient to enable 500 cycles, which was not previously examined. Regarding the capacity decay observed upon 500 consecutive cycles, a closer look at the differential capacity curves (Fig. S1 in Supporting Information) reveals that the capacity fading mostly affects the second sloping plateau (i.e., around 50 mV). This confirms that cycling at 100% depth of discharge (DOD) has a detrimental effect on cycling performance, as was observed in previous studies [34,49]. We are currently investigating the influence of capacity-limited cycling conditions as well as higher current densities on cycling stability of Si NW anodes in F-free IL electrolytes and the results will be published in future work.

In order to investigate the changes occurring at the electrode/electrolyte interface upon cycling, electrochemical impedance spectroscopy (EIS) was performed. Fig. 3a and b shows the Nyquist plot for the Si NW electrodes in ILE and ILE + VC, respectively, after the 1st and 20th cycle.

In both cases, the impedance spectrum consists of two semicircles at high to medium frequencies corresponding, respectively, to Li diffusion through the SEI (R_{SEI} | CPE1) and charge transfer at the electrode interface (R_{CT} | CPE2). Finally, a linear regime is observed at lower frequencies, i.e., below 6 Hz, associated with the contribution from Li^+ ions diffusion within the active material [45,50,51]. Considering the focus of this study on the interphase, the diffusive part of the spectra were excluded from the fitting of the impedance data. The equivalent circuit shown in Fig. 3c was used to model the impedance spectra (the resulting resistance values are summarized in Table S1). The extremely large charge transfer resistance (R_{CT}) in ILE (5102 Ω) explains the low lithiation capacity in the first cycle (1732 mA h g^{-1}). In fact, this can lead to rapid electrode potential drop to the set cut-off voltage before reaching the full lithiated state of Si. On the contrary, after addition of VC, the charge transfer resistance is decreased to 2587 Ω and the lithiation capacity increased to 4125 mA h g^{-1}.

Comparing the evolution of the spectra upon cycling, the effect of VC on the overall impedance is marked. The reduction of the charge transfer resistance (R_{CT}), which decreases from 2587 to 514 Ω upon the first 20 cycles in ILE + VC compared to a minimal decrease from 5102 to 4889 Ω in case of ILE, is evident. This decrease coincides with the establishment of the stable cycling regime observed in Fig. 2c and could be attributed to the increased electronic conductivity of the lithiated Si NWs [52]. The transformation of the discrete nanowires into a porous network providing a larger surface area for reaction (see the detailed post-mortem morphology study in section 3.2.1) could also explain such a behavior [41].

3.2. Post mortem characterization

3.2.1. SEM/EDX
The morphology of the Si NWs electrodes' surface after cycling in both ILE and ILE + VC was investigated via SEM (Fig. 4). For comparison, the SEM images of the pristine electrode are shown in Fig. 4a and b, which evidence a dense coverage of nanowires across the entire substrate, with the nanowire's surface appearing clean and with sharp boundaries. Notably, after the first cycle in ILE, the electrode's surface (Fig. 4c) remains relatively flat with micrometer-size deposits observed on the surface. Having a closer look at the Si NWs (Fig. 4d), they appear to be covered by a thick decomposition layer filling all the pores amongst them. The presence of such a thick layer could explain the extremely large impedance recorded for the electrode after the first cycle (see Fig. 3a). The large deposits observed on the electrode surface (Fig. 4c) are shown at higher magnification in Fig. S2 in Supporting Information. To further investigate the chemical composition of these deposits, energy dispersive X-ray (EDX) mapping was carried out. The deposits, which consist of carbon and nitrogen (Fig. S2 in Supporting Information), are attributable to the reduction product of ILE (i.e., LiDCA-Pyr$_{14}$TCM). Interestingly, the Si signal detected from these regions is drastically lower than from the rest of the surface, indicating a rather dense coverage of the nanowires in these spots. This suggests that the decomposition products are mostly formed on the stainless-steel current collector, which grow to cover the nanowires. Considering that the metallic current collector is more electronically conductive than Si, along with the highly porous nature of the nanowire coating, it is plausible to assume that the current collector is the preferred site for the electrolyte decomposition [53].

The influence of VC on the morphology of the electrode after the first cycle is observable in Fig. 4e. The surface appears rough and fragmented, indicative of volume changes during the (de-)alloying process. A more detailed look at the surface reveals island-like deposits similar to those observed in the case of ILE. The EDX mapping results (Fig. S3 in Supporting Information) are consistent with the electrolyte composition and deposition of SEI. However, the main signals detected differ from those of the sample cycled in ILE. In fact, in addition to the expected oxygen and carbon signals, a weaker signal from nitrogen was recorded confirming the role of VC in reducing the decomposition of ILE. At higher magnification (Fig. 4f), the well-preserved nanowires can be distinguished on the electrode surface.

After the 100th cycle, the electrode surface is evidently more ragged (Fig. 4g), indicative of repeated expansion/contraction of the underlying Si layer. Fig. 4i reveals a porous network of interconnected nano-ligaments after repeated cycling, which has been shown to play an essential role in high capacity retention over the course of hundreds of cycles [41,54]. It is notable that Fig. 4e–i also showcase the formation of a rather non-homogenous SEI layer. Such phenomenon is also reported by Luo et al. and can be attributed to several factors [55]. For example, the non-uniform distribution of Li amongst the Si NWs may lead to increased local conductivity in regions where more Li is accumulated, resulting in a not entirely homogenous SEI [55].

3.2.2. Solid electrolyte interphase (SEI) characterization
To gain further insight into the chemical composition of the SEI layer formed on the Si NW electrodes in ILE and ILE + VC, ex-situ XPS measurements were performed after the first galvanostatic cycle (i.e., delithiated state). High-resolution C 1s, N 1s, O 1s, Si 2p and Li 1s spectra of both electrodes (cycled in ILE and ILE + VC) were acquired from the
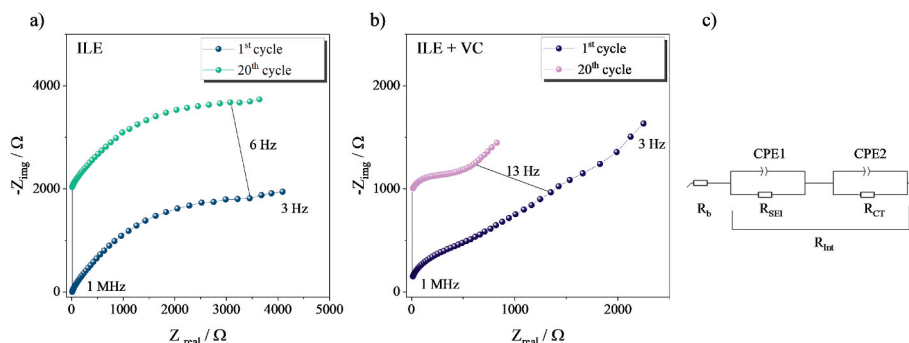

Fig. 3. Nyquist plots of Si electrodes in a) ILE and b) ILE + VC after the 1st and 20th cycles. (c) Equivalent circuit used to fit impedance data.
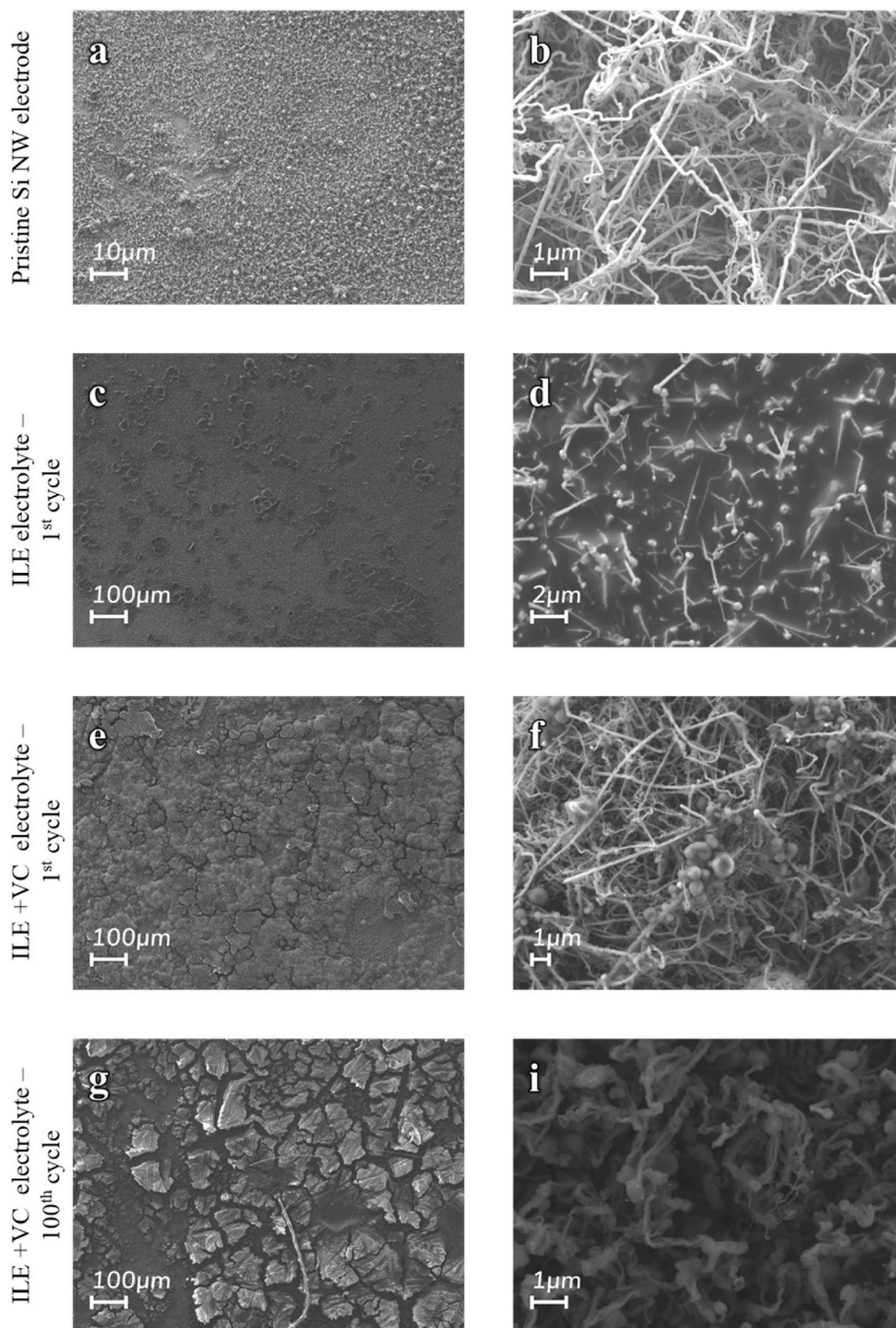
Fig. 4. Post mortem SEM images of Si NW electrodes (a–b) at pristine state, (c–d) after the first cycle in ILE, (e–f) after the first cycle in ILE + VC, and (g–i) after the 100th cycle in ILE + VC.

electrode surface and after 10, 20, 30, and 40 min of Ar$^+$ sputtering to provide the depth profiling of the surface layer. For each sample, the variation of relative elemental concentration was determined based on the survey scans, taking into account the sensitivity factor and the peak area of each element. Fig. 5 presents the atomic concentrations of each element with respect to increasing sputtering time. The survey scans of the cycled and pristine electrodes are provided in Figs. S4–S6 in Supporting Information. As shown in Fig. 5, in both cases, the main contribution comes from carbon-containing species (≈45%), which remains almost unchanged with sputtering time. It is noteworthy that for the electrode cycled in ILE + VC (Fig. 5b), the nitrogen concentration is remarkably lower than that recorded for the one in ILE, while the concentration of oxygen is higher. This clearly indicates the preferential

reduction of VC over the N-containing species present in the electrolyte, in agreement with the results obtained from the EDX mapping (see part 2.2.1). Compared to the gradual increase of the Si content in case of the electrode cycled in ILE (Fig. 5a), the Si content reaches a constant value of ≈3.6% after 30 min of sputtering in case of the ILE + VC sample. This suggests that the SEI layer formed in the ILE + VC is relatively thinner. It should be noted that due to inhomogeneous nature of the SEI layer, the thickness of the surface layer cannot be accurately determined. The slightly higher concentration of Li (about ≈25%) for the electrode cycled in the ILE is in agreement with its lower first cycle Coulombic efficiency compared to that cycled in ILE + VC (i.e., 42% and 48%, respectively). Interestingly, for both electrodes, the relative concentration of the elements remains almost constant during the extended sputtering time,
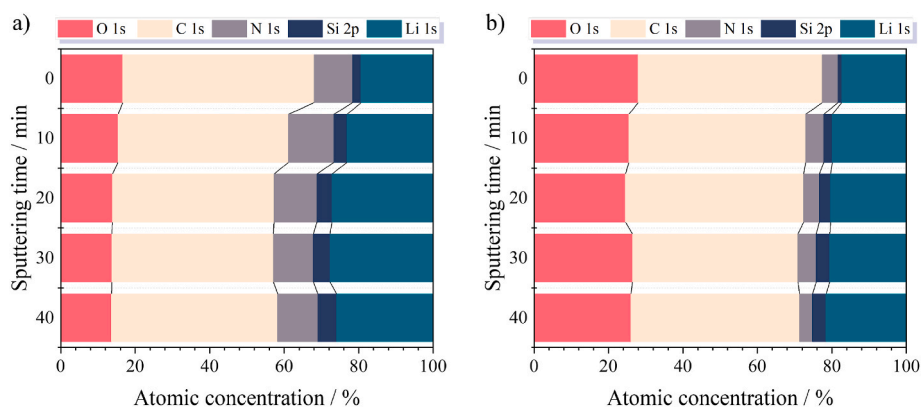
Fig. 5. Atomic concentration of the observed elements on the Si electrode surface after the first cycle in (a) ILE and (b) ILE + VC as a function of etching time.

indicating a relatively homogenous composition throughout the SEI layer thickness.

To obtain further insights into the nature of the SEI species and their depth distribution on the Si electrodes, the high-resolution N 1s and C 1s core spectra before and after 40 min of sputtering are presented in Figs. 6 and 7 for electrodes cycled in ILE and ILE + VC, respectively. To confirm the accuracy of the peak assignments and to correct for possible BE shifts associated with charging phenomena, the ΔBEs of identified phases were calculated and reported in Table S2 in Supporting Information [16, 33,56].

SEI composition in ILE. The N 1s spectrum of the outermost surface of the electrode (Fig. 6, top) displayed two sets of peaks. The first three peaks correspond to TCM (-C≡N) at 398.72 eV [16,57–61], DCA (-C-N$^-$-C-) at 399.56 eV [16,62], and N$^+$ at 402.01 eV [32,62–64], evidencing the presence of residual IL on the electrode surface, despite having been washed with DMC [16,62,63].

The second set of peaks appearing at 396.56 eV, 397.96 eV, and 400.40 eV, are attributed to LiC$_x$H$_y$N/Li$_3$N, -C-N- and/or LiCHN, and –N=C- double bond in a polymeric network, respectively [59–61,64,65]. These features are associated with reduction products of the electrolyte, where a polymeric network and Li$_3$N form due to reduction/polymerization of the DCA and TCM anions [15,66,67]. This is supported by previous studies on Li metal electrodes and confirmed by MD and DFT simulations [12,16]. Additionally, the presence of the double and triple bonds is testified by the observed π-excitation signal toward higher BE (about 4 eV) [12,60].

Upon sputtering, although the same components appear in the N 1s spectrum, the intensity of the three IL-related peaks (i.e., –C≡N at 398.84 eV, -C-N$^-$-C- at 399.60 eV, and N$^+$ at 401.95 eV) decreases, consistent with the removal of the residual IL along with the surface during etching. Additionally, the contribution of peaks ascribed to the decomposition products of the IL increases significantly. More precisely, the inorganic compounds such as Li$_3$N at 396.84 eV as well as compounds with -C-N- bond (at 398.14 eV) and –N=C- bond (at 400.60 eV)
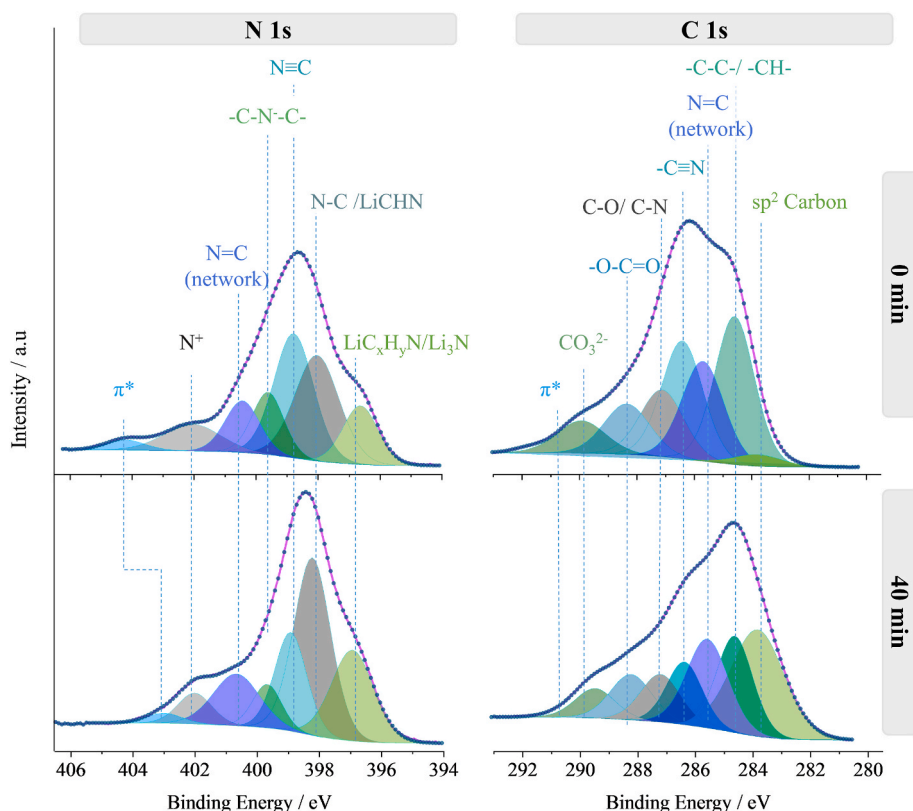

Fig. 6. High-resolution N 1s, and C 1s photoelectron spectra, before and after etching, of the Si electrode surface after the first cycle in ILE.
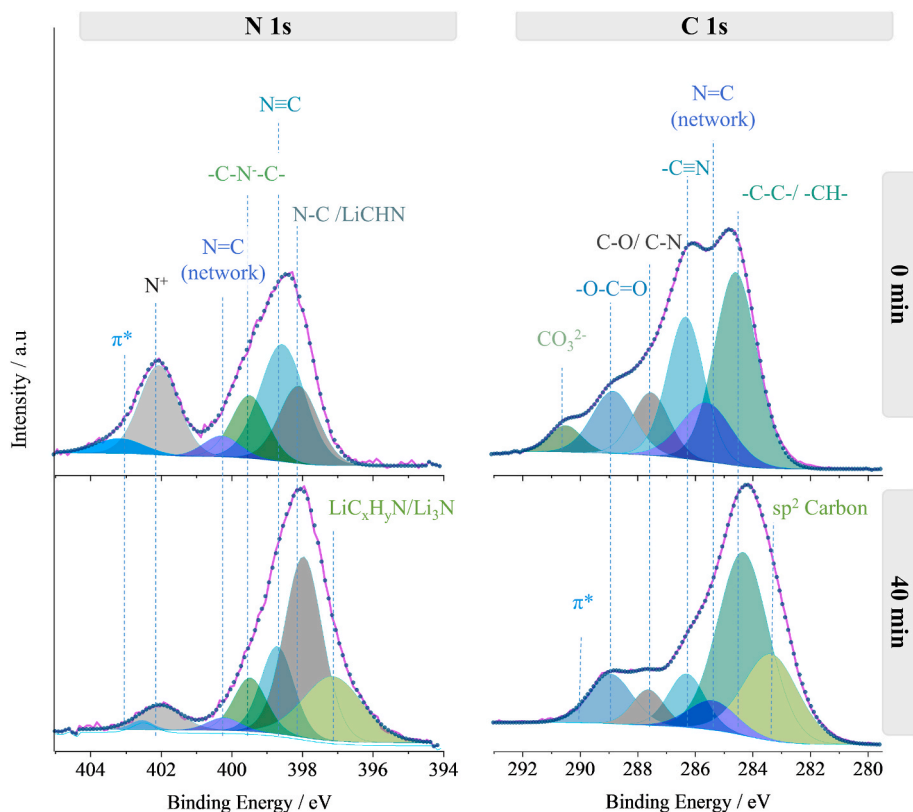
Fig. 7. High-resolution N 1s, and C 1s photoelectron spectra, before and after etching, of the Si electrode surface after the first cycle in ILE + VC.

characteristics appear to be dominating the inner layer, i.e., closer to the Si surface. It is worth noting the persistent presence of the IL signals most probably originates from the trapped IL in the porous structure of the Si nanowires.

The C 1s high-resolution spectrum of the outermost surface indicates the presence of C–C/C–H species at 284.53 eV [68,69], C≡N at 286.35 eV [59,61], and C–N at 287.07 eV [59,61,70], originating from degraded IL (i.e., DCA⁻, TCM⁻, and Pyr$_{14}^+$), as well as contributions from the IL persisting on the surface. Additionally, species with O–C=O character (possibly lithium alkylcarbonate) at 288.30 eV and CO_3^{2-} at 290.0 are detected, resulting from the reactions with DMC during the washing step [68,69,71]. In agreement with the conjugated C=N bonds observed in the N 1s spectra, the peak appearing at 285.63 eV also has the characteristics of carbon atoms having two single bonds with carbon/nitrogen and one double bond with nitrogen (note the peak at about 4 eV higher value attributed to π-excitation of the C≡N and C=N network). Furthermore, a small peak at 283.73 eV is seen on the surface, corresponding to graphitic sp^2 carbon. The amount of graphitic carbon present in the sample increases significantly with sputtering time and dominates the inner layer of the SEI, as shown in the C 1s spectrum (Fig. 6, bottom). Formation of such species indicates a complete reduction of the TCM anion, resulting in formation of graphitic carbon and Li$_3$N, which was in fact observed in the N 1s spectra [12,16].

The removal of IL along with the increase in the reduction/decomposition products of the electrolyte is also clearly seen in the C 1s spectrum after sputtering. This is in agreement with the results obtained from the N 1s spectrum, suggesting a higher degradation occurring close to the Si surface.

SEI composition in ILE + VC. Considering the N 1s spectrum (Fig. 7, top), the peaks associated with the IL, appearing at 398.50 eV (-C≡N), 399.43 eV (-C-N⁻-C-), and 402.01 eV (N⁺ of Pyr$_{14}^+$), are dominant, once again indicating for the presence of residual IL on the surface despite the washing step. However, in comparison with the electrode cycled in ILE, the spectrum is less broadened. More precisely, when VC is added, the

extent of electrolyte degradation appears to be diminished. This is evidenced by the peaks identified as -C-N- (at 398.03 eV) originating mostly from the Pyr$_{14}^+$ cation reduction, and N=C- double bond (at 400.23 eV) associated to the polymeric network (note the π-excitation signal at 403.13 eV) formed by reduction of the DCA and TCM anions. However, the peak associated with LiC$_x$H$_y$N/Li$_3$N (at 397.06 eV) only appears after sputtering along with removal of the IL (Fig. 7, bottom). Li$_3$N is known to be a critical SEI component providing high Li⁺ conductivity (6 mS cm⁻¹ at 25 °C) [72,73]. Interestingly, the inner layer of the SEI is dominated by Li$_3$N and species with -C-N- bond characteristics (possibly LiCHN), whereas the intensity of the peak corresponding to the C=N polymeric network decreases. It should be noted that when considering the difference in the total amount of nitrogen detected for this sample (i. e., almost one third of the detected amount for the ILE sample), the IL residue after sputtering is almost negligible and most likely arising from the ions still trapped in the porous structure of the electrode.

As mentioned previously, formation of nitride species (i.e., Li$_3$N) requires the complete reduction of the TCM and/or DCA anions, which consequently results in formation of graphitic carbon. This is also evidenced in the C 1s spectra before and after sputtering, where the sp^2 graphitic carbon peak at 283.3 eV appears only in the inner layer of the SEI (Fig. 7, bottom), in agreement with the N 1s spectra.

Similarly to the observed trend in the N 1s spectra, the intensity of the peak at ≈ 285.5 eV, associated with C=N bonds in a polymeric network, decreases with sputtering. This suggests that the formed SEI consists of two main layers: the outermost layer has polymeric characteristics, which can provide good mechanical stability and flexibility to withstand the volume changes of the underlying Si, while the inner layer is dominated by inorganic compounds such as Li$_3$N, delivering high Li-ion conductivity, as well as graphitic network that provide electronic conductivity.

Unexpectedly, the species identified in the C 1s spectra (Fig. 7) of the electrode cycled in ILE + VC are no different from those detected for the electrode cycled in ILE. In particular, besides the peak at 288.9 eV

associated with O–C═O carbon environment arising from decomposition of VC, no peaks ascribable to formation of polyVC (above 291 eV) could be detected [42,74,75]. This is perhaps due to the amount of added VC being so little with respect to the surface area of the sample, which can result in the amount of poly VC being too small for detection [51]. This could also be related to the decomposition potential of VC being much higher than that of the IL, causing its degradation products to be formed underneath the IL decomposition products, thus, requiring longer sputtering time for detection.

Regarding the graphitic carbon being located only in the inner layer, it is notable that in a previous study on the SEI formation of cyano-based IL on Li metal electrodes, we proposed that the graphitic carbon formation has a detrimental effect on the SEI formation process, due to its electronic conductivity promoting continuous electrolyte decomposition and thickening of the SEI [16]. However, due to the poorer electronic conductivity of Si compared to Li, the formation of the graphitic carbon might actually be beneficial in this case. According to XPS results, the graphitic carbon appears to be only present in the inner layer serving as a conductive coating for the Si active material, while being covered by the polymeric layer which prevents further decomposition of the electrolyte.

4. Conclusion

In this study, the fluorine-free IL, LiDCA-Pyr$_{14}$TCM (1–9 mole ratio) is investigated as electrolyte in combination with Si NW anodes. The galvanostatic cycling and electrochemical impedance spectroscopy tests of the Si anode with the IL electrolyte showed a poor cycling performance and extremely high interfacial resistance, suggesting the need for an SEI forming additive. In this regard, addition of the 5 wt% of VC to the electrolyte resulted in a highly reversible Si–Li alloying process with capacities of 1760 mA h g^{-1} after 200 cycles and 1500 mA h g^{-1} after 500 cycles, corresponding to 88% and 75% retention with respect to the second cycle delithiation capacity, respectively. The detailed study of the electrode/electrolyte interface during and after cycling revealed transformation of the nanowires into a porous network of interconnected nano-ligaments which, in turn, resulted in a decrease in interfacial resistance after prolonged cycling. On the basis of the XPS and EDX results, the addition of VC had a crucial role on reducing IL decomposition and consequently controlling the SEI thickness. The SEI formed in ILE exhibited a very homogenous composition throughout the thickness, whereas in case of ILE + VC the SEI consisted of two main layers. The inner layer appeared to be rich in graphitic carbon and inorganic compounds, enhancing the electronic conductivity of the Si substrate and Li-ion conductivity of the SEI, respectively. The outer layer, on the other hand, was rich in polymeric species, including groups with carbon-nitrogen single, double and triple bonds, which ensure a more cohesive and flexible surface film while serving as an insulating layer to prevent further electrolyte decomposition.

Authors contribution

S.P. supervised the work and provided funding. A.V. conceptualized and supervised the work, designed the experiments and discussed the data. N.K. designed and carried out experiments, analyzed and discussed the data and wrote the paper. M.Z. performed the XPS experiments, analyzed and discussed the data. H.G. and K.M.R. provided the Si nanowire electrodes. B.I and T.J.S.S provided the ionic liquids.

Declaration of competing interest

The authors declare that they have no known competing financial interests or personal relationships that could have appeared to influence the work reported in this paper.

References

[1] M. Armand, P. Axmann, D. Bresser, M. Copley, K. Edström, C. Ekberg, D. Guyomard, B. Lestriez, P. Novák, M. Petranikova, W. Porcher, S. Trabesinger, M. Wohlfahrt-Mehrens, H. Zhang, Lithium-ion batteries – current state of the art and anticipated developments, J. Power Sources 479 (2020), 228708, https://doi.org/10.1016/j.jpowsour.2020.228708.

[2] M. Armand, J.-M. Tarascon, Building better batteries, Nature 451 (2008) 652–657, https://doi.org/10.1038/451652a.

[3] Z.P. Cano, D. Banham, S. Ye, A. Hintennach, J. Lu, M. Fowler, Z. Chen, Batteries and fuel cells for emerging electric vehicle markets, Nat. Energy 3 (2018) 279–289, https://doi.org/10.1038/s41560-018-0108-1.

[4] D. Larcher, J.M. Tarascon, Towards greener and more sustainable batteries for electrical energy storage, Nat. Chem. 7 (2015) 19–29, https://doi.org/10.1038/nchem.2085.

[5] S. Chu, A. Majumdar, Opportunities and challenges for a sustainable energy future, Nature 488 (2012) 294–303, https://doi.org/10.1038/nature11475.

[6] B. Dunn, H. Kamath, J.M.J.-M. Tarascon, Electrical energy storage for the grid: a battery of choices, Science 334 (2011) 928–935, https://doi.org/10.1126/science.1212741, 80-.

[7] J. Kalhoff, G.G. Eshetu, D. Bresser, S. Passerini, Safer electrolytes for lithium-ion batteries: state of the art and perspectives, ChemSusChem 8 (2015) 2154–2175, https://doi.org/10.1002/cssc.201500284.

[8] H. Yang, G.V. Zhuang, P.N. Ross, Thermal stability of LiPF6 salt and Li-ion battery electrolytes containing LiPF6, J. Power Sources 161 (2006) 573–579, https://doi.org/10.1016/j.jpowsour.2006.03.058.

[9] S. Wilken, M. Treskow, J. Scheers, P. Johansson, P. Jacobsson, Initial stages of thermal decomposition of LiPF6-based lithium ion battery electrolytes by detailed Raman and NMR spectroscopy, RSC Adv. 3 (2013) 16359–16364, https://doi.org/10.1039/c3ra42611d.

[10] R. Wagner, M. Korth, B. Streipert, J. Kasnatscheew, D.R. Gallus, S. Brox, M. Amereller, I. Cekic-Laskovic, M. Winter, Impact of selected LiPF6 hydrolysis products on the high voltage stability of lithium-ion battery cells, ACS Appl. Mater. Interfaces 8 (2016) 30871–30878, https://doi.org/10.1021/acsami.6b09164.

[11] L. Zheng, H. Zhang, P. Cheng, Q. Ma, J. Liu, J. Nie, W. Feng, Z. Zhou, Li[(FSO2)(n-C4F9SO2)N] versus LiPF6 for graphite/LiCoO2 lithium-ion cells at both room and elevated temperatures: a comprehensive understanding with chemical, electrochemical and XPS analysis, Electrochim. Acta 196 (2016) 169–188, https://doi.org/10.1016/j.electacta.2016.02.152.

[12] H. Zhang, X. Judez, A. Santiago, M. Martinez-Ibañez, M.Á. Muñoz-Márquez, J. Carrasco, C. Li, G.G. Eshetu, M. Armand, Fluorine-free noble salt anion for high-performance all-solid-state lithium–sulfur batteries, Adv. Energy Mater. 9 (2019), 1900763, https://doi.org/10.1002/aenm.201900763.

[13] J. Scheers, D.H. Lim, J.K. Kim, E. Paillard, W.A. Henderson, P. Johansson, J. H. Ahn, P. Jacobsson, All fluorine-free lithium battery electrolytes, J. Power Sources 251 (2014) 451–458, https://doi.org/10.1016/j.jpowsour.2013.11.042.

[14] G. Hernández, J. Mindemark, A.J. Naylor, Y.C. Chien, D. Brandell, K. Edstrom, Elimination of fluorination: the influence of fluorine-free electrolytes on the performance of LiNi1/3Mn1/3Co1/3O2/silicon-graphite li-ion battery cells, ACS Sustain. Chem. Eng. 8 (2020) 10041–10052, https://doi.org/10.1021/acssuschemeng.0c01733.

[15] H. Yoon, G.H. Lane, Y. Shekibi, P.C. Howlett, M. Forsyth, A.S. Best, D. R. MacFarlane, Lithium electrochemistry and cycling behaviour of ionic liquids using cyano based anions, Energy Environ. Sci. 6 (2013) 979, https://doi.org/10.1039/c3ee23753b.

[16] N. Karimi, M. Zarrabeitia, A. Mariani, D. Gatti, A. Varzi, S. Passerini, Nonfluorinated ionic liquid electrolytes for lithium metal batteries: ionic conduction, electrochemistry, and interphase formation, Adv. Energy Mater. 11 (2021), 2003521, https://doi.org/10.1002/aenm.202003521.

[17] D.R. MacFarlane, M. Forsyth, E.I. Izgorodina, A.P. Abbott, G. Annat, K. Fraser, On the concept of ionicity in ionic liquids, Phys. Chem. Chem. Phys. 11 (2009) 4962–4967, https://doi.org/10.1039/b900201d.

[18] D.R. Macfarlane, N. Tachikawa, M. Forsyth, J.M. Pringle, P.C. Howlett, G.D. Elliott, J.H. Davis, M. Watanabe, P. Simon, C.A. Angell, Energy applications of ionic

liquids, Energy Environ. Sci. 7 (2014) 232–250, https://doi.org/10.1039/c3ee42099j.

[19] X. Wang, M. Salari, D. en Jiang, J. Chapman Varela, B. Anasori, D.J. Wesolowski, S. Dai, M.W. Grinstaff, Y. Gogotsi, Electrode material–ionic liquid coupling for electrochemical energy storage, Nat. Rev. Mater. 5 (2020) 787–808, https://doi.org/10.1038/s41578-020-0218-9.

[20] D.R. MacFarlane, S.A. Forsyth, J. Golding, G.B. Deacon, Ionic liquids based on imidazolium and pyrrolidinium salts of the tricyanomethanide anion, Green Chem. 4 (2002) 444–448, https://doi.org/10.1039/b205641k.

[21] D.R. MacFarlane, J. Golding, S. Forsyth, M. Forsyth, G.B. Deacon, Low viscosity ionic liquids based on organic salts of the dicyanamide anion, Chem. Commun. 16 (2001) 1430–1431, https://doi.org/10.1039/b103064g.

[22] S. Shen, S. Fang, L. Qu, D. Luo, L. Yang, S.I. Hirano, Low-viscosity ether-functionalized pyrazolium ionic liquids based on dicyanamide anions: properties and application as electrolytes for lithium metal batteries, RSC Adv. 5 (2015) 93888–93899, https://doi.org/10.1039/c5ra17539a.

[23] M.N. Obrovac, V.L. Chevrier, Alloy negative electrodes for Li-ion batteries, Chem. Rev. 114 (2014) 11444–11502, https://doi.org/10.1021/cr500207g.

[24] G.G. Eshetu, H. Zhang, X. Judez, H. Adenusi, M. Armand, S. Passerini, E. Figgemeier, Production of high-energy Li-ion batteries comprising silicon-containing anodes and insertion-type cathodes, Nat. Commun. 12 (2021) 1–14, https://doi.org/10.1038/s41467-021-25334-8.

[25] J. Asenbauer, T. Eisenmann, M. Kuenzel, A. Kazzazi, Z. Chen, D. Bresser, The success story of graphite as a lithium-ion anode material – fundamentals, remaining challenges, and recent developments including silicon (oxide) composites, Sustain. Energy Fuels 4 (2020) 5387–5416, https://doi.org/10.1039/D0SE00175A.

[26] L.K. Willenberg, P. Dechent, G. Fuchs, D.U. Sauer, E. Figgemeier, High-precision monitoring of volume change of commercial lithium-ion batteries by using strain gauges, Sustain. Times 12 (2020), https://doi.org/10.3390/su12020557.

[27] E. Mullane, T. Kennedy, H. Geaney, C. Dickinson, K.M. Ryan, Synthesis of tin catalyzed silicon and germanium nanowires in a solvent-vapor system and optimization of the seed/nanowire interface for dual lithium cycling, Chem. Mater. 25 (2013) 1816–1822, https://doi.org/10.1021/cm400367v.

[28] K. Stokes, T. Kennedy, G.T. Kim, H. Geaney, D. Storan, F. Laffir, G.B. Appetecchi, S. Passerini, K.M. Ryan, Influence of carbonate-based additives on the electrochemical performance of Si NW anodes cycled in an ionic liquid electrolyte, Nano Lett. 20 (2020) 7011–7019, https://doi.org/10.1021/acs.nanolett.0c01774.

[29] P.C. Howlett, N. Brack, A.F. Hollenkamp, M. Forsyth, D.R. MacFarlane, Characterization of the lithium surface in N-methyl-N-alkylpyrrolidinium bis (trifluoromethanesulfonyl)amide room-temperature ionic liquid electrolytes, J. Electrochem. Soc. 153 (2006) A595, https://doi.org/10.1149/1.2164726.

[30] G.M.A. Girard, M. Hilder, D. Nucciarone, K. Whitbread, S. Zavorine, M. Moser, M. Forsyth, D.R. MacFarlane, P.C. Howlett, Role of Li concentration and the SEI layer in enabling high performance Li metal electrodes using a phosphonium bis (fluorosulfonyl)imide ionic liquid, J. Phys. Chem. C 121 (2017) 21087–21095, https://doi.org/10.1021/acs.jpcc.7b01929.

[31] G.M.A. Girard, M. Hilder, N. Dupre, D. Guyomard, D. Nucciarone, K. Whitbread, S. Zavorine, M. Moser, M. Forsyth, D.R. MacFarlane, P.C. Howlett, Spectroscopic characterization of the SEI layer formed on lithium metal electrodes in phosphonium bis(fluorosulfonyl)imide ionic liquid electrolytes, ACS Appl. Mater. Interfaces 10 (2018) 6719–6729, https://doi.org/10.1021/acsami.7b18183.

[32] R.K. Blundell, P. Licence, Quaternary ammonium and phosphonium based ionic liquids: a comparison of common anions, Phys. Chem. Chem. Phys. 16 (2014) 15278–15288, https://doi.org/10.1039/c4cp01901f.

[33] K.N. Wood, G. Teeter, XPS on Li-Battery-Related compounds: analysis of inorganic SEI phases and a methodology for charge correction, ACS Appl. Energy Mater. 1 (2018) 4493–4504, https://doi.org/10.1021/acsaem.8b00406.

[34] M.N. Obrovac, L.J. Krause, Reversible cycling of crystalline silicon powder, J. Electrochem. Soc. 154 (2007) A103, https://doi.org/10.1149/1.2402112.

[35] J. Li, J.R. Dahn, An in situ X-ray diffraction study of the reaction of Li with crystalline Si, J. Electrochem. Soc. 154 (2007) A156, https://doi.org/10.1149/1.2409862.

[36] D.S.M. Iaboni, M.N. Obrovac, Li15Si4 formation in silicon thin film negative electrodes, J. Electrochem. Soc. 163 (2016) A255–A261, https://doi.org/10.1149/2.0551602jes.

[37] X.H. Liu, Y. Liu, A. Kushima, S. Zhang, T. Zhu, J. Li, J.Y. Huang, In situ TEM experiments of electrochemical lithiation and delithiation of individual nanostructures, Adv. Energy Mater. 2 (2012) 722–741, https://doi.org/10.1002/aenm.201200024.

[38] M. Gu, Z. Wang, J.G. Connell, D.E. Perea, L.J. Lauhon, F. Gao, C. Wang, Electronic origin for the phase transition from amorphous LixSi to crystalline Li15Si4, ACS Nano 7 (2013) 6303–6309, https://doi.org/10.1021/nn402349j.

[39] M.R. Zamfir, H.T. Nguyen, E. Moyen, Y.H. Lee, D. Pribat, Silicon nanowires for Li-based battery anodes: a review, J. Mater. Chem. A. 1 (2013) 9566, https://doi.org/10.1039/c3ta11714f.

[40] M. Montanino, M. Moreno, M. Carewska, G. Maresca, E. Simonetti, R. Lo Presti, F. Alessandrini, G.B. Appetecchi, Mixed organic compound-ionic liquid electrolytes for lithium battery electrolyte systems, J. Power Sources 269 (2014) 608–615, https://doi.org/10.1016/j.powsour.2014.07.027.

[41] G.-T. Kim, T. Kennedy, M. Brandon, H. Geaney, K.M. Ryan, S. Passerini, G. B. Appetecchi, Behavior of germanium and silicon nanowire anodes with ionic liquid electrolytes, ACS Nano 11 (2017) 5933–5943, https://doi.org/10.1021/acsnano.7b01705.

[42] H. Ota, Y. Sakata, A. Inoue, S. Yamaguchi, Analysis of vinylene carbonate derived SEI layers on graphite anode, J. Electrochem. Soc. 151 (2004) 1659–1669, https://doi.org/10.1149/1.1785795.

[43] J. Graetz, C.C. Ahn, R. Yazami, B. Fultz, Highly reversible lithium storage in nanostructured silicon, Electrochem. Solid State Lett. 6 (2003), https://doi.org/10.1149/1.1596917.

[44] M. Green, E. Fielder, B. Scrosati, M. Wachtler, J. Serra Moreno, Structured silicon anodes for lithium battery applications, Electrochem. Solid State Lett. 6 (2003), https://doi.org/10.1149/1.1563094.

[45] V. Chakrapani, F. Rusli, M.A. Filler, P.A. Kohl, Quaternary ammonium ionic liquid electrolyte for a silicon nanowire-based lithium ion battery, J. Phys. Chem. C 115 (2011) 22048–22053, https://doi.org/10.1021/jp207605w.

[46] M.T. McDowell, S.W. Lee, I. Ryu, H. Wu, W.D. Nix, J.W. Choi, Y. Cui, Novel size and surface oxide effects in silicon nanowires as lithium battery anodes, Nano Lett. 11 (2011) 4018–4025, https://doi.org/10.1021/nl202630n.

[47] C.K. Chan, R.N. Patel, M.J. O'Connell, B.A. Korgel, Y. Cui, M.J.O. Connell, B. A. Korgel, Y.C. Ḱ, Solution-grown silicon nanowires for lithium-ion battery anodes, ACS Nano 4 (2010) 1443–1450, https://doi.org/10.1021/nn901409q.

[48] C.K. Chan, H. Peng, G.A.O. Liu, K. McIlwrath, X.F. Zhang, R.A. Huggins, Y.I. Cui, High-performance lithium battery anodes using silicon nanowires, Nat. Nanotechnol. 3 (2008) 31–35, https://doi.org/10.1038/nnano.2007.411.

[49] C.K. Chan, R. Ruffo, S.S. Hong, R.A. Huggins, Y. Cui, Structural and electrochemical study of the reaction of lithium with silicon nanowires, J. Power Sources 189 (2009) 34–39, https://doi.org/10.1016/j.jpowsour.2008.12.047.

[50] R. Ruffo, S.S. Hong, C.K. Chan, R.A. Huggins, Y. Cui, Impedance analysis of silicon nanowire lithium ion battery anodes, J. Phys. Chem. C 113 (2009) 11390–11398, https://doi.org/10.1021/jp901594g.

[51] L. Chen, K. Wang, X. Xie, J. Xie, Effect of vinylene carbonate (VC) as electrolyte additive on electrochemical performance of Si film anode for lithium ion batteries, J. Power Sources 174 (2007) 538–543, https://doi.org/10.1016/j.jpowsour.2007.06.149.

[52] H. Wu, G. Yu, L. Pan, N. Liu, M.T. McDowell, Z. Bao, Y. Cui, Stable Li-ion battery anodes by in-situ polymerization of conducting hydrogel to conformally coat silicon nanoparticles, Nat. Commun. 4 (2013) 1943, https://doi.org/10.1038/ncomms2941.

[53] C.K. Chan, R. Ruffo, S.S. Hong, Y. Cui, Surface chemistry and morphology of the solid electrolyte interphase on silicon nanowire lithium-ion battery anodes, J. Power Sources 189 (2009) 1132–1140, https://doi.org/10.1016/j.jpowsour.2009.01.007.

[54] T. Kennedy, M. Brandon, F. Laffir, K.M. Ryan, Understanding the influence of electrolyte additives on the electrochemical performance and morphology evolution of silicon nanowire based lithium-ion battery anodes, J. Power Sources 359 (2017) 601–610, https://doi.org/10.1016/j.jpowsour.2017.05.093.

[55] F. Luo, G. Chu, X. Xia, B. Liu, J. Zheng, J. Li, H. Li, C. Gu, L. Chen, Thick solid electrolyte interphases grown on silicon nanocone anodes during slow cycling and their negative effects on the performance of Li-ion batteries, Nanoscale 7 (2015) 7651–7658, https://doi.org/10.1039/c5nr00045a.

[56] B. Philippe, R. Dedryvère, J. Allouche, F. Lindgren, M. Gorgoi, H. Rensmo, D. Gonbeau, K. Edström, K. Edstro, R. Dedryvère, J. Allouche, F. Lindgren, M. Gorgoi, H. Rensmo, D. Gonbeau, K. Edström, Nanosilicon electrodes for lithium-ion batteries: interfacial mechanisms studied by hard and soft X-ray photoelectron spectroscopy, Chem. Mater. 24 (2012) 1107–1115, https://doi.org/10.1021/cm2034195.

[57] F. Rossi, B. Andre, A. van Veen, P.E. Miinarends, H. Schut, F. Labohm, H. Dunlop, M.P. Delnlancke, K. Hubbard, Physical properties of a-C: N films produced by ion beam assisted deposition, J. Mater. Res. 9 (1994) 2440–2449, https://doi.org/10.1557/JMR.1994.2440.

[58] M. Ricci, M. Trinquecoste, F. Auguste, R. Canet, P. Delhaes, C. Guimon, G. Pfister-Guillouzo, B. Nysten, J.P. Issi, Relationship between the structural organization and the physical properties of PECVD nitrogenated carbons, J. Mater. Res. 8 (1993) 480–488, https://doi.org/10.1557/JMR.1993.0480.

[59] S. Bhattacharyya, J. Hong, G. Turban, Determination of the structure of amorphous nitrogenated carbon films by combined Raman and x-ray photoemission spectroscopy, J. Appl. Phys. 83 (1998) 3917–3919, https://doi.org/10.1063/1.367312.

[60] A.P. Dementjev, A. De Graaf, M.C.M. Van de Sanden, K.I. Maslakov, A.V. Naumkin, A.A. Serov, X-ray photoelectron spectroscopy reference data for identification of the C3N4 phase in carbon-nitrogen films, Diam. Relat. Mater. 9 (2000) 1904–1907, https://doi.org/10.1016/S0925-9635(00)00345-9.

[61] S. Bhattacharyya, C. Cardinaud, G. Turban, Spectroscopic determination of the structure of amorphous nitrogenated carbon films, J. Appl. Phys. 83 (1998) 4491–4500, https://doi.org/10.1063/1.367211.

[62] P.C. Howlett, N. Brack, A.F. Hollenkamp, M. Forsyth, D.R. MacFarlane, Characterization of the lithium surface in N-methyl-N-alkylpyrrolidinium Bis (trifluoromethanesulfonyl)amide room-temperature ionic liquid electrolytes, J. Electrochem. Soc. 153 (2006), https://doi.org/10.1149/1.2164726.

[63] J. Sun, A. O'Dell, M. Armand, P.C. Howlett, M. Forsyth, Anion-Derived solid-electrolyte interphase enables long life Na-ion batteries using superconcentrated ionic liquid electrolytes, ACS Energy Lett. 6 (2021) 2481–2490, https://doi.org/10.1021/acsenergylett.1c00816.

[64] F. Buchner, K. Forster-Tonigold, M. Bozorgchenani, A. Gross, R.J. Behm, Interaction of a self-assembled ionic liquid layer with graphite(0001): a combined experimental and theoretical study, J. Phys. Chem. Lett. 7 (2016) 226–233, https://doi.org/10.1021/acs.jpclett.5b02449.

[65] F. Buchner, K. Forster-Tonigold, J. Kim, J. Bansmann, A. Groß, R.J. Behm, Interaction between Li, ultrathin adsorbed ionic liquid films, and CoO(111) thin

films: a model study of the Solid|Electrolyte interphase formation, Chem. Mater. 31 (2019) 5537–5549, https://doi.org/10.1021/acs.chemmater.9b01253.

[66] T.J. Wooster, K.M. Johanson, K.J. Fraser, D.R. MacFarlane, J.L. Scott, Thermal degradation of cyano containing ionic liquids, Green Chem. 8 (2006) 691–696, https://doi.org/10.1039/b606395k.

[67] J.P. Paraknowitsch, J. Zhang, D. Su, A. Thomas, M. Antonietti, Ionic liquids as precursors for nitrogen-doped graphitic carbon, Adv. Mater. 22 (2010) 87–92, https://doi.org/10.1002/adma.200900965.

[68] B. Philippe, R. Dedryvère, M. Gorgoi, H. Rensmo, D. Gonbeau, K. Edström, Improved performances of nanosilicon electrodes using the salt LiFSI: a photoelectron spectroscopy study, J. Am. Chem. Soc. 135 (2013) 9829–9842, https://doi.org/10.1021/ja403082s.

[69] R.I.R. Blyth, H. Buqa, F.P. Netzer, M.G. Ramsey, J.O. Besenhard, P. Golob, M. Winter, XPS studies of graphite electrode materials for lithium ion batteries, Appl. Surf. Sci. 167 (2000) 99–106, https://doi.org/10.1016/S0169-4332(00)00525-0.

[70] C.C. Nguyen, S.W. Song, Characterization of SEI layer formed on high performance Si-Cu anode in ionic liquid battery electrolyte, Electrochem, Commun. Now. 12 (2010) 1593–1595, https://doi.org/10.1016/j.elecom.2010.09.003.

[71] L. Martin, H. Martinez, M. Ulldemolins, B. Pecquenard, F. Le Cras, F. Le Cras, Evolution of the Si electrode/electrolyte interface in lithium batteries characterized by XPS and AFM techniques: the influence of vinylene carbonate additive, Solid State Ionics 215 (2012) 36–44, https://doi.org/10.1016/j.ssi.2012.03.042.

[72] A. Wang, S. Kadam, H. Li, S. Shi, Y. Qi, Review on modeling of the anode solid electrolyte interphase (SEI) for lithium-ion batteries, Npj Comput. Mater. 4 (2018) 15, https://doi.org/10.1038/s41524-018-0064-0.

[73] U.v. Alpen, A. Rabenau, G.H. Talat, Ionic conductivity in Li 3 N single crystals, Appl. Phys. Lett. 30 (1977) 621–623, https://doi.org/10.1063/1.89283.

[74] L. El Ouatani, R. Dedryvère, C. Siret, P. Biensan, S. Reynaud, P. Iratçabal, D. Gonbeau, The effect of vinylene carbonate additive on surface film formation on both electrodes in Li-ion batteries, J. Electrochem. Soc. 156 (2009) A103, https://doi.org/10.1149/1.3029674.

[75] L. Madec, J. Xia, R. Petibon, K.J. Nelson, J.P. Sun, I.G. Hill, J.R. Dahn, Effect of sulfate electrolyte additives on LiNi1/3Mn1/3Co1/3O2/graphite pouch cell lifetime: correlation between xps surface studies and electrochemical test results, J. Phys. Chem. C 118 (2014) 29608–29622, https://doi.org/10.1021/jp509731y.